

---

---

# Image-Derived Input Function for Assessment of $^{18}\text{F}$ -FDG Uptake by the Inflamed Lung

Tobias Schroeder<sup>1</sup>, Marcos F. Vidal Melo<sup>1</sup>, Guido Musch<sup>1</sup>, R. Scott Harris<sup>2</sup>, Jose G. Venegas<sup>1</sup>, and Tilo Winkler<sup>1</sup>

<sup>1</sup>Department of Anesthesia and Critical Care, Massachusetts General Hospital and Harvard Medical School, Boston, Massachusetts; and <sup>2</sup>Department of Medicine (Pulmonary and Critical Care Unit), Massachusetts General Hospital and Harvard Medical School, Boston, Massachusetts

---

Pulmonary uptake of  $^{18}\text{F}$ -FDG assessed with PET has been used to quantify the metabolic activity of inflammatory cells in the lung. This assessment involves modeling of tracer kinetics and knowledge of a time-activity curve in pulmonary artery plasma as an input function, usually acquired by manual blood sampling. This paper presents and validates a method to accurately derive an input function from a blood-pool region of interest (ROI) defined in dynamic PET images. **Methods:** The method is based on a 2-parameter model describing the activity of blood and that from spillover into the time-activity curve for the ROI. The model parameters are determined using an iterative algorithm, with 2 blood samples used to calibrate the raw PET-derived activity data. We validated both the 2-parameter model and the method to derive a quantitative input function from ROIs defined for the cavities of the right and left heart and for the descending aorta by comparing them against the time-activity curve obtained by manual blood sampling from the pulmonary artery in lungs with acute inflammation. **Results:** The model accurately described the time-activity curve from sampled blood. The 2-sample calibration method provided an efficient algorithm to derive input functions that were virtually identical to those sampled manually, including the fast kinetics of the early phase. The  $^{18}\text{F}$ -FDG uptake rates in acutely injured lungs obtained using this method correlated well with those obtained exclusively using manual blood sampling ( $R^2 > 0.993$ ). Within some bounds, the model was found quite insensitive to the timing of calibration blood samples or the exact definition of the blood-pool ROIs. **Conclusion:** Using 2 mixed venous blood samples, the method accurately assesses the entire time course of the pulmonary  $^{18}\text{F}$ -FDG input function and does not require the precise geometry of a specific blood-pool ROI or a population-based input function. This method may substantially facilitate studies involving modeling of pulmonary  $^{18}\text{F}$ -FDG in patients with viral or bacterial infections, pulmonary fibrosis, and chronic obstructive pulmonary disease.

**Key Words:** PET; Massachusetts General Hospital;  $^{18}\text{F}$ -FDG; acute lung injury; inflammation

**J Nucl Med 2007; 48:1889–1896**  
DOI: 10.2967/jnumed.107.041079

**P**ET imaging of  $^{18}\text{F}$ -FDG is increasingly used to assess the metabolic activity of pulmonary inflammatory cells (1–7). The uptake rate of  $^{18}\text{F}$ -FDG by tissue can be computed using either compartmental models (8) or a graphical technique (9). A prerequisite for either analysis is knowledge of the input function to the system in the form of a plasma time-activity curve. Acquisition of such an input function typically involves sequential blood sampling, a process that is invasive, is prone to measurement artifacts, exposes the clinical staff to radiation and blood, and adds costly laboratory procedures. To avoid or minimize manual blood sampling, substantial effort has been devoted to developing alternative techniques, which have successfully been applied to estimate  $^{18}\text{F}$ -FDG uptake in tumors and brain. Some of these techniques involve population-based assumptions about the input function (10–13), whereas others directly estimate the input function from blood-pool regions of interest (ROIs) in the PET images (14–18).

However, population-based assumptions about the input function are not available for  $^{18}\text{F}$ -FDG uptake by the inflamed nonneoplastic lung and may vary for different types of pulmonary inflammation. Also, estimates of the input function from blood-pool ROIs are affected by partial-volume effects and by activity spillover from the heart or inflamed pulmonary tissues. Moreover, in contrast to brain, heart, or solid tumor tissues, where the blood-to-tissue fraction is low, blood volume in the lung may account for as much as half the parenchymal volume. As a result, the blood compartment is a dominant source of lung  $^{18}\text{F}$ -FDG activity, particularly early after tracer injection. Because early-phase kinetics affect estimates of distribution volumes and rapid rate constants, accurate assessment of the early-phase input function might be crucial for characterizing the inflamed lung. Although techniques to reduce blood sampling are available, they seem to have limited accuracy in describing the early-phase input function (13,14,17–19) or are unable to assess the early phase of the input function at all (10–12). Techniques involving image-derived assessment of the early input function either neglected partial-volume effects (18) and activity spillover artifacts (15) or mathematically corrected for these artifacts

---

Received Feb. 26, 2007; revision accepted Jul. 30, 2007.  
For correspondence or reprints contact: Tobias Schroeder, Department of Anesthesia and Critical Care, Massachusetts General Hospital, 55 Fruit St., Boston, MA 02114.  
E-mail: tschroeder@partners.org  
COPYRIGHT © 2007 by the Society of Nuclear Medicine, Inc.

by measuring the anatomic dimensions of the blood-pool ROI used (16). Alternatively, spillover from myocardium into the left ventricle was calculated on the basis of the difference in activity between the arterial and ROI-derived curves at the last sampled point, and a standard myocardial wall thickness was assumed to correct for partial-volume effect (17).

In this paper, we present and validate a method of obtaining an image-derived input function for compartmental modeling of  $^{18}\text{F}$ -FDG kinetics in the lung. The method is based on a 2-parameter model of the blood-pool ROI that accounts for partial-volume and spillover artifacts, is not restricted to a blood-pool ROI with precisely known geometry, and does not assume a population-based input function.

## MATERIALS AND METHODS

### Model-Based Computation of a PET Image-Derived Input Function

We model the PET signal from a blood-pool ROI ( $C_{\text{ROI}}(t)$ ) by 2 compartments. One accounts for  $^{18}\text{F}$ -FDG activity from blood plasma ( $C_p(t)$ ), and the other for spillover activity from tracer that accumulates in tissue surrounding the ROI. We define a recovery coefficient ( $RC$ ) quantifying a geometric partial-volume effect and a spillover coefficient ( $SC$ ) to quantify activity spillover from phosphorylated  $^{18}\text{F}$ -FDG in the surrounding tissue.  $SC$  is a function of the  $^{18}\text{F}$ -FDG uptake rate in surrounding tissue, the geometry of the ROI, and the spatial resolution of the imaging instrument.  $C_{\text{ROI}}(t)$  is expressed as

$$C_{\text{ROI}}(t) = RC C_p(t) + SC \int C_p(\tau) d\tau, \quad \text{Eq. 1}$$

where the integral describes the time course of  $^{18}\text{F}$ -FDG phosphorylation in surrounding tissue as a function of  $^{18}\text{F}$ -FDG availability in blood. This simplification is expected to yield a time course that is sufficiently accurate for the purpose of spillover correction. Dividing both sides of Equation 1 by  $C_p(t)$  yields an instantaneous calibration factor between  $C_{\text{ROI}}(t)$  and  $C_p(t)$ :

$$\frac{C_{\text{ROI}}(t)}{C_p(t)} = RC + SC \frac{\int C_p(\tau) d\tau}{C_p(t)}. \quad \text{Eq. 2}$$

The structure of this linear equation is identical to the equation used in the Patlak method (20). However, in addition to a different interpretation of the slope in our model ( $SC$ ), the ordinate intercept (termed initial volume of distribution in the Patlak method) represents here the  $RC$ , which depends on ROI geometry and spatial resolution characteristics of the PET camera. By assuming that  $RC$  and  $SC$  are constant during the imaging period and measuring plasma activity with 2 blood samples,  $C_p(t_1)$  and  $C_p(t_2)$ , taken at time points  $t_1$  and  $t_2$ , we can write Equation 2 as an equation system:

$$\begin{bmatrix} C_{\text{ROI}}(t_1)/C_p(t_1) \\ C_{\text{ROI}}(t_2)/C_p(t_2) \end{bmatrix} = RC + SC \begin{bmatrix} \int_{\tau=0}^{t_1} C_p(\tau) d\tau / C_p(t_1) \\ \int_{\tau=0}^{t_2} C_p(\tau) d\tau / C_p(t_2) \end{bmatrix}. \quad \text{Eq. 3}$$

To solve Equation 3 for  $RC$  and  $SC$ , we need the integral of the unknown time course of  $C_p(t)$ , which is obtained using the

iterative algorithm summarized in the flow chart in Figure 1. The algorithm begins by assuming that  $C_{\text{ROI}}(t)$  is an initial estimate of  $C_p(t)$  ( $\tilde{C}_p(t)_{[0]}$ ), which is used to calculate the integral in Equation 3 as

$$\int_{\tau=0}^{t_n} C_p(\tau) d\tau = \sum_{k=1}^n \Delta t_k \tilde{C}_p(t_k)_{[0]}, \quad \text{Eq. 4}$$

where  $\Delta t_k$  was the duration of the  $k^{\text{th}}$  image frame and  $n$  refers to the  $n^{\text{th}}$  time point of the integral. Then, solving Equation 3 provides current ( $i^{\text{th}}$ ) estimates of  $RC$  and  $SC$  ( $RC_{[i]}$  and  $SC_{[i]}$ ), which are used to obtain the next estimate of  $C_p(t)$ ,  $\tilde{C}_p(t)_{[i]}$ , as

$$\tilde{C}_p(t)_{[i]} = \frac{C_{\text{ROI}}(t) - SC_{[i]} \int \tilde{C}_p(\tau)_{[i-1]} d\tau}{RC_{[i]}}. \quad \text{Eq. 5}$$

This procedure is repeated until estimates of plasma activity at  $t_1$  and  $t_2$  converge to measured values (i.e.,  $\tilde{C}_p(t_1)_{[i]} = C_p(t_1)$  and  $\tilde{C}_p(t_2)_{[i]} = C_p(t_2)$ ), with an error ( $e$ ) defined as

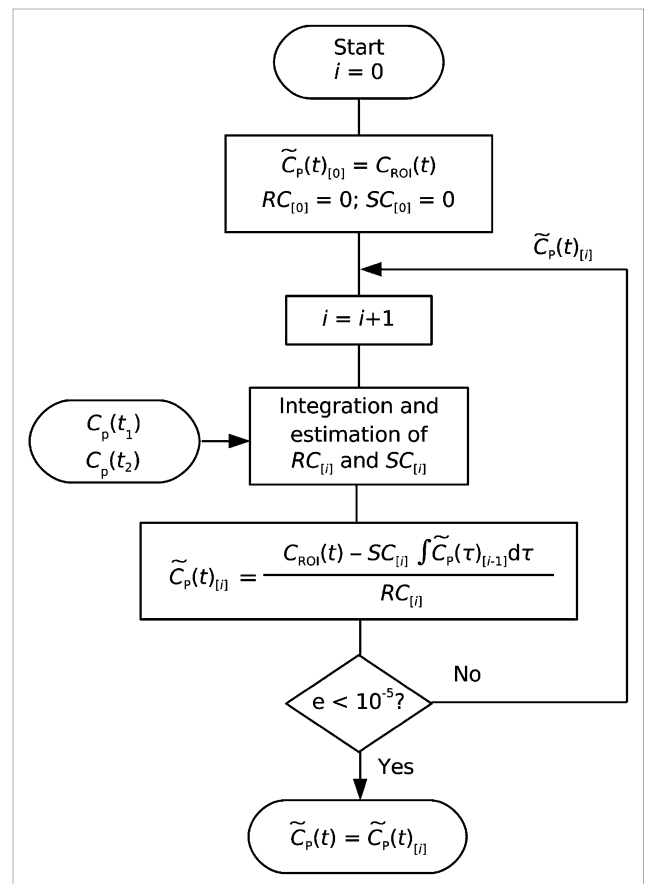


**FIGURE 1.** Iterative algorithm for calculating model-adjusted input function ( $\tilde{C}_p(t)$ ). Method is based on 2-compartment model. PET signal from blood-pool ROI is separated in blood and activity spillover component by estimating  $RC$  and  $SC$ . Index  $[i]$  refers to number of iterations.  $C_{\text{ROI}}(t)$  = raw PET signal from blood-pool ROI;  $\tilde{C}_p(t)_{[i]}$  =  $i^{\text{th}}$  estimate of plasma activity;  $C_p(t_1)$  and  $C_p(t_2)$  = calibration measurements of plasma activity, obtained at times  $t_1$  and  $t_2$ .

$$e = \sqrt{\frac{(\tilde{C}_p(t_1)_{[i]} - C_p(t_1))^2 + (\tilde{C}_p(t_2)_{[i]} - C_p(t_2))^2}{(C_p(t_1) + C_p(t_2))/2}} \quad \text{Eq. 6}$$

of less than  $10^5$ .

### Experimental Data

We analyzed data from previous studies of pulmonary inflammation in sheep. These studies, in which pulmonary  $^{18}\text{F}$ -FDG kinetics were measured with dynamic PET and pulmonary artery blood sampling, included 5 sheep exposed to unilateral smoke inhalation (3) and 10 sheep exposed to unilateral injurious ventilation (2). Specific details about animal preparation can be found in the original publications. In brief, a Swan–Ganz catheter (7.5 French) was advanced to the pulmonary artery. The proximal (central venous) port was used for administration of the radioisotope and the distal port for sampling of pulmonary artery blood. Each sheep was positioned prone in the PET camera (Scanditronix PC4096; GE Healthcare), with the most caudal slice adjacent to the diaphragmatic dome to maximize the imaged lung volume (21). The camera collected 15 transverse cross-sectional slices of 6.5-mm thickness over a 9.7-cm-long axial field.

PET data recorded during intravenous bolus injection of  $^{13}\text{N}$  saline solution ( $344 \pm 96$  MBq dissolved in 30 mL) were used to define the ROI for the right heart (RH) cavities. These PET data were acquired to assess regional pulmonary perfusion in the previous studies (2,3), in which simultaneously with the start of the  $^{13}\text{N}$ -saline injection, image acquisition was started with an initial framing rate of 2.5 s per frame.

After the  $^{13}\text{N}$  was cleared from the lungs, a bolus of  $^{18}\text{F}$ -FDG ( $\sim 370$  MBq) was injected at a constant rate over 1 min into the superior vena cava, followed by a flush of saline at the same rate. Acquisition of a series of PET images was started simultaneously with  $^{18}\text{F}$ -FDG injection ( $t = 0$ ). The protocol consisted of acquiring consecutive images for a total of 75 min ( $6 \times 30$  s,  $7 \times 1$  min,  $15 \times 2$  min,  $1 \times 5$  min, and  $3 \times 10$  min). An additional study was conducted with a modified protocol involving a prolonged tracer injection time (90 s) and an increased initial framing rate (8 frames over the first 2 min after tracer injection).

PET images were reconstructed in an interpolated matrix of  $128 \times 128 \times 15$  voxels, each with a size of  $2 \times 2 \times 6.5$  mm. The time course of  $^{18}\text{F}$ -FDG activity in blood plasma was measured from sequential 1-mL samples of pulmonary artery blood in a well counter cross-calibrated with the PET camera. The intervals between blood samples were  $11 \times 15$  s,  $4 \times 30$  s,  $5 \times 1$  min,  $11 \times 5$  min, and  $1 \times 10$  min. Thus, for the first 4.5 min, the time points of blood sampling were synchronized with the mid-frame time points of PET. For  $t > 4.5$  min, the plasma measurements were linearly

interpolated and values coinciding with the mid-frame time points of the PET frames were derived from the interpolated data.

Three ROIs were defined in the images delineating the descending aorta, RH cavities, and left heart (LH) cavities. The RH-cavity ROI was identified by thresholding the regional activity of  $^{13}\text{N}$  during the first 5 s after  $^{13}\text{N}$ -saline injection. During this time  $^{13}\text{N}$  is confined mostly to the RH cavities and pulmonary arteries, and only a minor amount has diffused into the alveolar gas volume (Fig. 2A). The LH-cavity and aorta ROIs were generated using the  $^{18}\text{F}$ -FDG image data. To delineate the aorta, we applied a threshold of about 50% to regional  $^{18}\text{F}$ -FDG activity from 1.5 to 2.5 min after the start of injection (Fig. 2B). Regional activity in the interval from 55 to 65 min after  $^{18}\text{F}$ -FDG bolus injection was used to identify the wall of the left ventricle (Fig. 2C). The ROI over the LH cavities was manually drawn along the inner border of the left ventricular wall by the use of custom-made image-processing software. In cases in which myocardial uptake was low, the LH-cavity masks were generated from the early injection images.

### Comparison Between Model-Adjusted Input Function and Manual Blood Samples

The relative mean squared error (*mse*) between manually sampled plasma activity ( $C_p(t)$ ) and the time course of the model-adjusted input function ( $\tilde{C}_p(t)$ ), excluding the first 2 blood samples, was calculated from all points at which PET image frames coincided with blood samples:

$$mse = \frac{1}{N-2} \sum_{k=3}^N \left( \frac{\tilde{C}_p(t_k) - C_p(t_k)}{C_p(t_k)} \right)^2, \quad \text{Eq. 7}$$

with  $n = 32$ . The first 2 measurements were excluded because, at this early phase, some of the manually sampled data were skipped or corrupted by timing errors.

To evaluate the influence of the first calibration sample time on *mse*, its timing ( $t_1$ ) was systematically varied within the interval from 1.75 to 25 min, using time points corresponding to mid-frame time points. The timing of the second calibration sample was fixed at  $t_2 = 50$  min. An identical procedure was followed for each of the 3 ROIs, and the corresponding *mse* data were compared with the nonparametric Wilcoxon signed rank test. The level of significance was  $P < 0.05$ . To test the robustness of our method to blood-pool ROI definition, the ROIs were systematically dilated, and the model-adjusted input function was computed for each increment in ROI volume. Bland–Altman plots (22) were used to illustrate the agreement between  $K_i$  values computed with

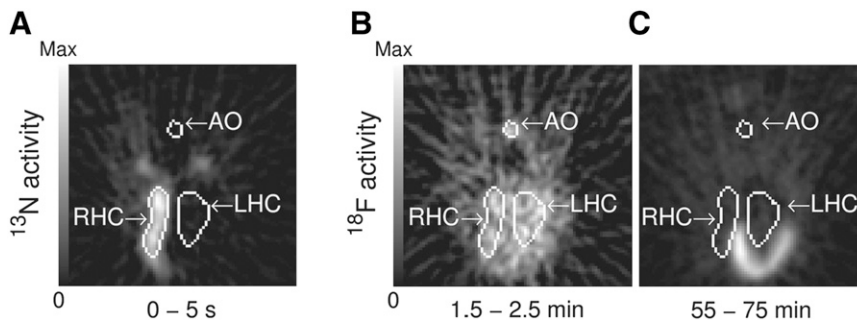


**FIGURE 2.** Delineation (white outlines) of blood-pool ROIs in descending aorta (AO) and in RH cavities (RHC) and LH cavities (LHC) on representative image slice: regional activity after intravenous single-bolus injection of  $^{13}\text{N}$ -nitrogen dissolved in saline (A) and  $^{18}\text{F}$ -FDG activity, on identical scale, shortly after tracer injection and at end of imaging (B and C, respectively). The 3 ROIs are shown together only for illustration purposes.

manual blood sampling and either raw or model-adjusted input functions.

### Patlak Graphical Analysis

The pulmonary uptake rate of  $^{18}\text{F}$ -FDG ( $K_i$ ) for injured and control lungs was calculated by Patlak graphical analysis (20), starting 15 min after tracer injection, using the manually sampled input function, raw PET signals from the blood-pool ROIs, and input functions generated with the 2-compartment model.

### RESULTS

The linear model formulated by Equation 2 provided an excellent approximation of the PET signals from the blood-pool ROIs (Fig. 3A). Using the iterative algorithm (Fig. 1), we found that estimates of  $RC$  and  $SC$  converged within  $\leq 6$  iterations to their final values (Fig. 4). For the ROI volumes used,  $RC$  was on average highest for the LH cavities and lowest for the aorta (Table 1).  $SC$  was about the same for all 3 ROIs. With increasing ROI volume, average  $SC$  increased for all 3 ROIs and was highest for the LH cavities and lowest for the RH cavities for ROI volumes  $> 70$  mL (Fig. 3B). Figure 3C depicts average  $SC$  values normalized by  $(1 - RC)$  as a function of blood ROI volume. Values of  $SC/(1 - RC)$  were consistently highest for the LH cavities and smallest for the aorta for ROI volumes  $\leq 75$  mL. For  $1.75 \text{ min} \leq t_1 \leq 25 \text{ min}$ , the  $mse$  between model-adjusted input function and manually sampled input function was on average lowest for the LH cavities and highest for the RH cavities (Fig. 5). Also within this period, mean  $mse$  for the LH cavities was fairly insensitive to  $t_1$ , with a minimum at  $t_1 = 4.5 \text{ min}$ .

The raw PET signal from the blood-pool ROIs systematically underestimated the manually sampled input function during the early phase and overestimated it during the late phase (Fig. 6A). In contrast, the model-adjusted input functions provided excellent agreement with the manually sampled data for most time points, although during the peak phase ( $t < 2 \text{ min}$ ) manual blood samples differed slightly from the model-adjusted input function (insets of Fig. 6). Similar results were obtained for experimental data with prolonged tracer injections and higher framing rates during the early phase (Fig. 6B).

When raw PET signals from the blood-pool ROIs were used as input functions, Patlak  $K_i$  values were systemati-

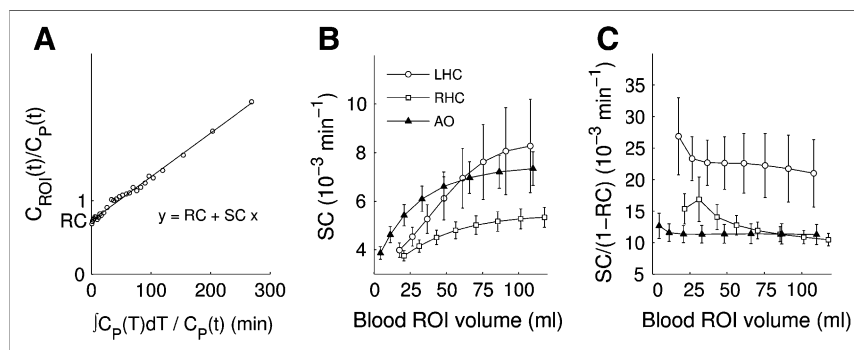
cally underestimated, compared with those calculated with the manually sampled input functions (Fig. 7A; Table 2). This bias was particularly pronounced in lungs with high values of  $K_i$  (Fig. 7B). In contrast, with model-adjusted input functions,  $K_i$  values were highly correlated with those obtained with manual blood sampling (Table 2; Fig. 7C), without any bias between the 2 methods (Fig. 7D).

### DISCUSSION

We have presented here a model-adjusted input function that, requiring only 2 calibration blood samples, agrees very well with the manually sampled pulmonary artery input function and leads to unbiased estimates of  $^{18}\text{F}$ -FDG uptake in the normal and inflamed lung. The method is rather insensitive to the collection time of the first calibration sample, which can be chosen to be between 3.5 and 25 min after the start of tracer injection when a second calibration sample is taken at 50 min from injection. More important, the approach performs well with blood-pool ROIs affected by activity spillover or partial volume, without requiring a priori knowledge of a population-based input function or of the exact ROI anatomy.

Our basic model assumption was that the instantaneous calibration factor ( $C_{\text{ROI}}(t)/C_p(t)$ ) could be described by the simple linear function in Equation 2 to adjust the PET ROI data for spillover and partial-volume artifacts. This assumption is clearly supported by the linearity of the plot between the  $C_{\text{ROI}}/C_p$  and the normalized integral of  $C_p$  obtained from the experimental PET and blood sampling data (Fig. 3A). In that plot, the y-axis intercept corresponds to an  $RC$  and the slope of the function to an  $SC$ .  $SC$  is a function of the  $^{18}\text{F}$ -FDG uptake rate in surrounding tissue, and like  $RC$ , is also a function of ROI geometry and the spatial resolution of the imaging instrument, which our algorithm automatically adjusts for each individual ROI. The geometric effects on  $SC$  are demonstrated by its dependence on blood ROI volume (Fig. 3B), where  $SC$  became larger for the LH cavities than for the aorta at increasing ROI volume as more activity from the myocardium was included in the LH-cavity mask. Furthermore, if the factor  $(1 - RC)$  is taken as a rough estimate of the geometric and spatial resolution effects on  $SC$ , normalizing  $SC$  by this factor would approximate the  $^{18}\text{F}$ -FDG uptake

**FIGURE 3.** Evaluation of model fit and effect of ROI volume on estimated parameter  $SC$ : representative model fit according to Equation 2 for dynamic PET data measured in blood-pool ROI over LH cavities (A), average  $SC$  obtained for blood-pool ROIs of varying size, illustrating how algorithm adjusts  $SC$  to different conditions (B); normalized  $SC/(1 - RC)$ , illustrating differences in  $^{18}\text{F}$ -FDG uptake rates (C). Error bars are  $\pm 1 \times \text{SE}$ . ROIs with lowest volume were used for analyses.



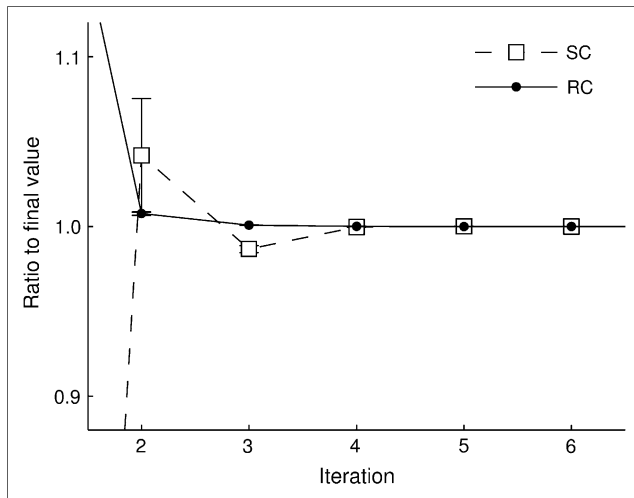


**FIGURE 4.** Convergence of iterative algorithm (Fig. 1) for model parameters *RC* and *SC*. Plot was generated for blood-pool ROIs in LH. Error bars are  $\pm 1 \times \text{SE}$ .

rate in surrounding tissues.  $SC/(1 - RC)$  was relatively independent of ROI volume and substantially larger (and more variable) for the LH cavities, compared with that of the aorta (Fig. 3C). This finding is consistent with the expectation of higher  $^{18}\text{F}$ -FDG uptake in the myocardium than surrounding the aorta. Therefore, if ROI design is aimed at minimizing the amount of tissue in the blood-pool ROIs, Equation 2 seems to be a robust and practical approach to adjusting the time-activity curve from the blood-pool ROIs for partial-volume and spillover effects.

A second model assumption was that the concentrations of  $^{18}\text{F}$ -FDG in whole blood and plasma were in equilibrium. This assumption seems justifiable given that  $^{18}\text{F}$ -FDG equilibrates almost instantaneously between plasma and erythrocytes (23), as supported by the fact that the model-adjusted input function agreed well with manually sampled blood plasma activity during the first few minutes after injection.

Our approach involves 2 user inputs in the computation of the input function. One is the delineation of the blood-pool ROIs, and another the selection of time points for withdrawing calibration blood samples. The method presented here was found rather insensitive to both of these steps. ROI delineation can be a subjective process, requiring individual adjustment of threshold values and manual

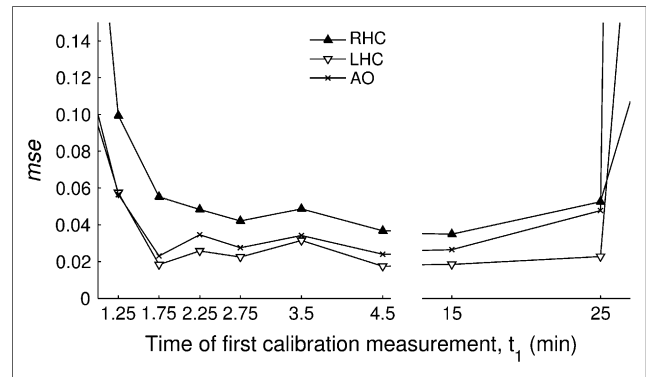


**FIGURE 5.** *mse* between model-adjusted input function and manually sampled input function as function of time point of first calibration measurement,  $t_1$ . Plot shows results for blood-pool ROIs in RH and LH cavities (RHC and LHC, respectively) and descending aorta (AO). Values are out of scale for  $t_1 = 0.25$  min,  $t_1 = 0.75$  min, and  $t_1 > 25$  min (not shown).

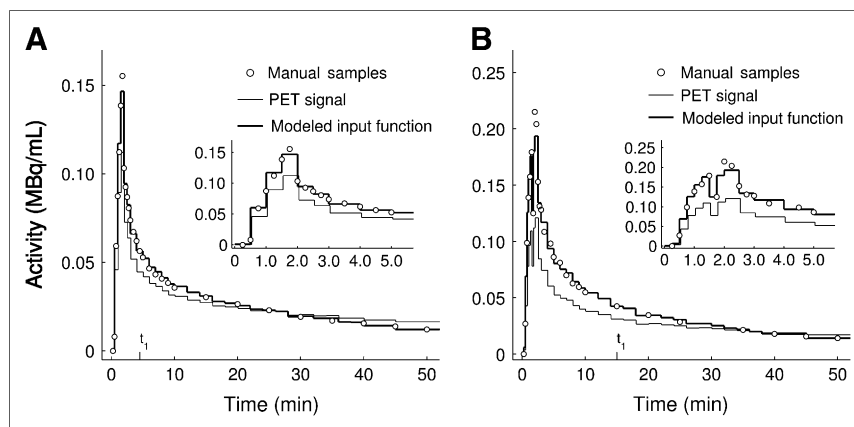
editing to account for imaging artifacts. However, because the model parameters were automatically adjusted for an ROI, it was sufficient to define a rough outline of the ROI without precise knowledge of myocardium or vessel anatomy. Indeed, when we generated model-adjusted input functions for ROIs of different sizes to calculate  $K_i$  values in smoke-exposed and control lungs, these values changed by less than 0.5% despite a 5-fold difference in defined ROI volumes. Our results also suggest that for Patlak analysis, any of the 3 blood-pool ROIs studied could be used with our model-adjusted input function. However, for estimating individual rate constants of a more complex compartmental model, such as that of Sokoloff et al. (24), defining ROIs over the LH cavities or aorta could be preferable given the lower *mse* values they yield, compared with the ROI over the RH cavities. This is advantageous because defining the LH cavities and aorta does not require a  $^{13}\text{N}$ -saline injection.

The second user input in calculating the model-adjusted input function is the timing of the calibration measurements. There are 2 competing effects for this timing. To maximize the robustness of linear regression in Equation 3, one should choose  $t_1$  and  $t_2$  to be as far apart as possible. On the other hand, the closer  $t_1$  is to the time of tracer bolus injection, the greater is the chance of measurement artifacts during the manual blood sampling because of the rapid tracer kinetics taking place. Because the *mse* between manually sampled and model-adjusted input functions was relatively constant for a wide range of initial calibration sample timings ( $t_1$ ), it is feasible to choose the first calibration sample over a wide range of times without substantially affecting the robustness of the model-adjusted input function. This feasibility was also demonstrated for a study with a modified tracer injection rate, where the variation in peak tracer activity was particularly high because of a delay between the end of tracer injection and the start of a flush removing remaining tracer from the injection system.

**TABLE 1**  
Volume of Blood-Pool ROIs and Estimates of Model Parameters *RC* and *SC*

ROI	ROI volume (mL)	<i>RC</i>	<i>SC</i> ( $\text{min}^{-1}$ )
RH cavities	$20.6 \pm 12.0$	$0.69 \pm 0.18$	$0.0038 \pm 0.0009$
LH cavities	$17.5 \pm 8.3$	$0.78 \pm 0.11$	$0.0039 \pm 0.0011$
Descending aorta	$4.4 \pm 1.3$	$0.64 \pm 0.11$	$0.0039 \pm 0.0011$

**FIGURE 6.** Comparison of activity in manual blood samples of pulmonary artery plasma, raw PET signal from blood-pool ROI in LH cavities, and model-adjusted input function: example of calibration measurements at  $t_1 = 4.5$  min and  $t_2 = 50$  min (A); example of longer tracer injection time (90 s instead of 1 min) and shorter initial PET frames (15 s instead of 30 s), with  $t_1 = 15$  min and  $t_2 = 50$  min (B). Discontinuity during peak was due to delay between end of tracer injection and flush of saline used to remove remaining tracer from infusion system.



Although the use of the model-adjusted input function reduces the total number of blood samples, sampling of mixed venous blood is still involved. It is reasonable to expect that for large values of  $t_1$ , plasma activity in the peripheral veins could sufficiently approximate plasma activity in mixed venous blood. Future studies are needed to validate the use of peripheral venous blood in combination with our model.

For compartmental modeling of  $^{18}\text{F}$ -FDG kinetics in pulmonary inflammatory states, an accurate estimate of the early-phase input function is desirable. Previously published techniques (11,13,15,18,19,25) may be limited for

this purpose. For instance, in the presence of significant myocardial  $^{18}\text{F}$ -FDG uptake, the uncorrected image signal from an ROI in the LH was found to substantially differ from the manually sampled input function during the early phase, and the tumor metabolic rate of glucose was underestimated by as much as 12% with this raw image-derived input function (18). In accordance with our analysis, those errors could explain the substantial bias in  $K_i$  when an unadjusted PET signal from a blood-pool ROI is used as the input function.

Takikawa et al. (13) calculated a population-based input function by averaging manually sampled input functions that

**FIGURE 7.** Evaluation of  $^{18}\text{F}$ -FDG uptake rates ( $K_i$ ) for raw image-derived input functions and for model-adjusted input functions in comparison to  $K_i$  values obtained with manual blood sampling.  $K_i$  values include exposed and nonexposed lungs and were obtained with input functions from blood-pool ROIs in RH cavities (RHC), LH cavities (LHC), and aorta (AO). Shown are  $K_i$  obtained with raw image-derived input functions (A) and corresponding Bland-Altman plot (B), and  $K_i$  values calculated with model-adjusted input functions (C) and corresponding Bland-Altman plot (D). All values are in  $10^{-3}$  mL blood/mL lung/min. Parameters of linear regression analysis are summarized in Table 2.

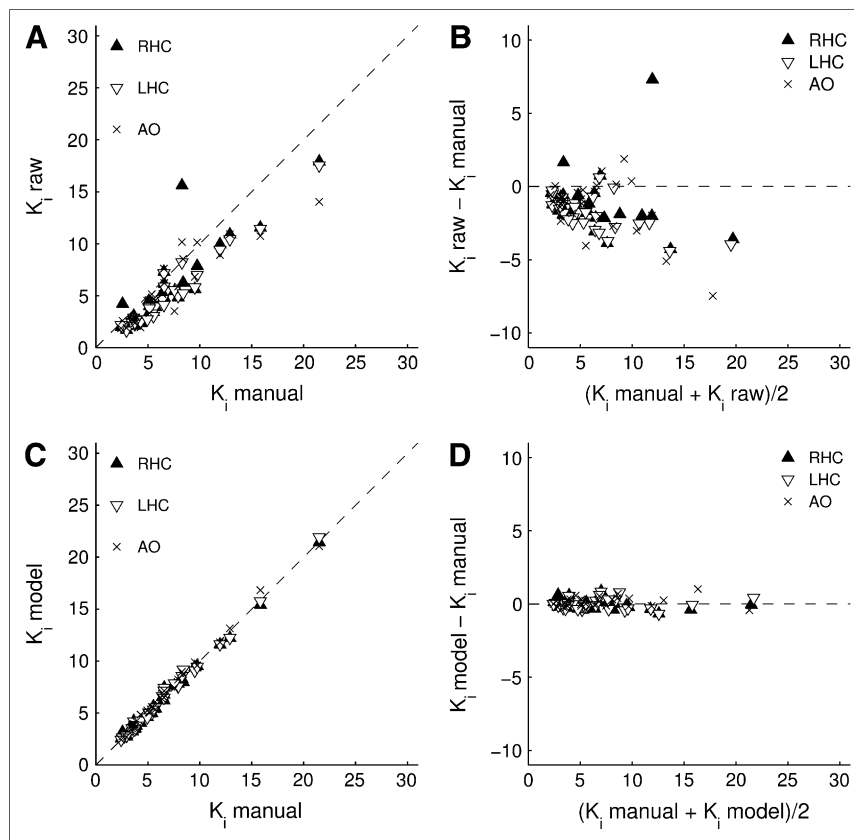


TABLE 2

Regression Analysis of  $^{18}\text{F}$ -FDG Uptake Rates ( $K_i$ ) for Model-Adjusted Input Functions and for Raw Image-Derived Input Functions in Comparison to Manual Blood Sampling (Figs. 7A and 7C)

Input function	ROI	Slope of regression line	y-Intercept of regression line	$R^2$
Model-adjusted	RH cavities	0.979	0.065	0.994
	LH cavities	1.003	-0.035	0.993
	Descending aorta	1.006	0.080	0.994
Raw image-derived	RH cavities	0.839	-0.194	0.782
	LH cavities	0.806	-0.468	0.945
	Descending aorta	0.712	0.636	0.837

$R^2$  = coefficient of determination.

were obtained in a particular population. The disadvantage of this approach is that the individual input function of a subject may be very different from the population-based input function, and it is unclear if population-based input functions can be used to accurately estimate parameters reflecting early-phase tracer kinetics.

Another method used to estimate the plasma time-activity curve described clearance of  $^{18}\text{F}$ -FDG from the blood by a sum of 3 decaying exponential functions that have to be known a priori for a specific population (11). However, this method fails to account for early-phase tracer kinetics. Yet another method has derived the arterial input function from an ROI over the descending aorta, by assuming a signal free from activity spillover (15). This freedom from spillover cannot be guaranteed in the case of increased uptake in lung regions, as encountered during acute lung inflammation (2-4,6). In fact, we found that the SC for the aorta was on average as large as that of the other 2 ROIs. Other elegant methods to estimate an image-derived input function require a priori assumptions (17) or measurements (16) of myocardial anatomy and are restricted to ROIs within the left ventricle. Our method circumvents these requirements, although it involves the withdrawal of 2 calibration blood samples. For applications in brain, Naganawa et al. (25) developed a method that extracts the input function by independent-component analysis based on the fact that cerebral blood volume is very small (2%-4%) and that there is only a small fraction of voxels (1%-2%) with a substantial blood content. These conditions are clearly not met in the lung, where blood volume can be as much as 20% of a voxel (7).

## CONCLUSION

Our model-adjusted method to estimate a PET-derived input function allows accurate reconstruction of the time-activity curve in pulmonary artery blood for modeling pulmonary uptake of centrally injected  $^{18}\text{F}$ -FDG. This method requires only 2 blood samples, the first of which can be taken as late as 25 min, with the second sample taken 50 min after tracer injection. Delineation of the

blood-pool ROI is less critical than in other techniques, because the model implicitly adjusts the data for partial-volume and activity spillover effects. This approach is expected to substantially facilitate studies involving compartmental modeling of  $^{18}\text{F}$ -FDG kinetics of the inflamed lung, possibly also including patients with viral or bacterial infections, pulmonary fibrosis, and chronic obstructive pulmonary disease.

## ACKNOWLEDGMENTS

This work was funded by NIH grants RO1-HL-086827, HL-056879, HL-068011, and HL-076464. One of the authors was supported in part by the German Academic Exchange Service (DAAD) and by Roland Ernst Stiftung.

## REFERENCES

- Chen DL, Schuster DP. Positron emission tomography with [ $^{18}\text{F}$ ]fluorodeoxyglucose to evaluate neutrophil kinetics during acute lung injury. *Am J Physiol Lung Cell Mol Physiol*. 2004;286:L834-L840.
- Musch G, Venegas JG, Bellani G, et al. Regional gas exchange and cellular metabolic activity in ventilator-induced lung injury. *Anesthesiology*. 2007;106:723-735.
- Schroeder T, Vidal Melo MF, Musch G, Harris RS, Winkler T, Venegas JG. PET imaging of regional  $^{18}\text{F}$ -FDG uptake and lung function following cigarette smoke inhalation. *J Nucl Med*. 2007;48:413-419.
- Zhou Z, Kozlowski J, Goodrich AL, Markman N, Chen DL, Schuster DP. Molecular imaging of lung glucose uptake after endotoxin in mice. *Am J Physiol Lung Cell Mol Physiol*. 2005;289:L760-L768.
- Jones HA, Clark RJ, Rhodes CG, Schofield JB, Krausz T, Haslett C. In vivo measurement of neutrophil activity in experimental lung inflammation. *Am J Respir Crit Care Med*. 1994;149:1635-1639.
- Jones HA, Srisikandan S, Peters AM, et al. Dissociation of neutrophil emigration and metabolic activity in lobar pneumonia and bronchiectasis. *Eur Respir J*. 1997;10:795-803.
- Chen DL, Mintun MA, Schuster DP. Comparison of methods to quantitate  $^{18}\text{F}$ -FDG uptake with PET during experimental acute lung injury. *J Nucl Med*. 2004;45:1583-1590.
- Phelps ME, Huang SC, Hoffman EJ, Selin C, Sokoloff L, Kuhl DE. Tomographic measurement of local cerebral glucose metabolic rate in humans with (F-18)2-fluoro-2-deoxy-D-glucose: validation of method. *Ann Neurol*. 1979;6:371-388.
- Patlak CS, Blasberg RG, Fenstermacher JD. Graphical evaluation of blood-to-brain transfer constants from multiple-time uptake data. *J Cereb Blood Flow Metab*. 1983;3:1-7.
- Sundaram SK, Freedman NM, Carrasquillo JA, et al. Simplified kinetic analysis of tumor  $^{18}\text{F}$ -FDG uptake: a dynamic approach. *J Nucl Med*. 2004;45:1328-1333.

11. Hunter GJ, Hamberg LM, Alpert NM, Choi NC, Fischman AJ. Simplified measurement of deoxyglucose utilization rate. *J Nucl Med.* 1996;37:950–955.
12. Wong WH, Hicks K. A clinically practical method to acquire parametric images of unidirectional metabolic rates and blood spaces. *J Nucl Med.* 1994;35:1206–1212.
13. Takikawa S, Dhawan V, Spetsieris P, et al. Noninvasive quantitative fluoro-deoxyglucose PET studies with an estimated input function derived from a population-based arterial blood curve. *Radiology.* 1993;188:131–136.
14. Chen K, Bandy D, Reiman E, et al. Noninvasive quantification of the cerebral metabolic rate for glucose using positron emission tomography, <sup>18</sup>F-fluoro-2-deoxyglucose, the Patlak method, and an image-derived input function. *J Cereb Blood Flow Metab.* 1998;18:716–723.
15. Ohtake T, Kosaka N, Watanabe T, et al. Noninvasive method to obtain input function for measuring tissue glucose utilization of thoracic and abdominal organs. *J Nucl Med.* 1991;32:1432–1438.
16. Henze E, Huang SC, Ratib O, Hoffman E, Phelps ME, Schelbert HR. Measurements of regional tissue and blood-pool radiotracer concentrations from serial tomographic images of the heart. *J Nucl Med.* 1983;24:987–996.
17. Gambhir SS, Schwaiger M, Huang SC, et al. Simple noninvasive quantification method for measuring myocardial glucose utilization in humans employing positron emission tomography and fluorine-18 deoxyglucose. *J Nucl Med.* 1989;30:359–366.
18. Geus-Oei LF, Visser EP, Krabbe PF, et al. Comparison of image-derived and arterial input functions for estimating the rate of glucose metabolism in therapy-monitoring <sup>18</sup>F-FDG PET studies. *J Nucl Med.* 2006;47:945–949.
19. van der Weerd AP, Klein LJ, Boellaard R, Visser CA, Visser FC, Lammertsma AA. Image-derived input functions for determination of MRGlu in cardiac <sup>18</sup>F-FDG PET scans. *J Nucl Med.* 2001;42:1622–1629.
20. Patlak CS, Blasberg RG. Graphical evaluation of blood-to-brain transfer constants from multiple-time uptake data: generalizations. *J Cereb Blood Flow Metab.* 1985;5:584–590.
21. Vidal Melo MF, Layfield D, Harris RS, et al. Quantification of regional ventilation-perfusion ratios with PET. *J Nucl Med.* 2003;44:1982–1991.
22. Bland JM, Altman DG. Comparing methods of measurement: why plotting difference against standard method is misleading. *Lancet.* 1995;346:1085–1087.
23. Nahmias C, Wahl LM, Amano S, Asselin MC, Chirakal R. Equilibration of 6-[<sup>18</sup>F]fluoro-L-m-tyrosine between plasma and erythrocytes. *J Nucl Med.* 2000;41:1636–1641.
24. Sokoloff L, Reivich M, Kennedy C, et al. The [<sup>14</sup>C]deoxyglucose method for the measurement of local cerebral glucose utilization: theory, procedure, and normal values in the conscious and anesthetized albino rat. *J Neurochem.* 1977;28:897–916.
25. Naganawa M, Kimura Y, Ishii K, Oda K, Ishiwata K, Matani A. Extraction of a plasma time-activity curve from dynamic brain PET images based on independent component analysis. *IEEE Trans Biomed Eng.* 2005;52:201–210.